Regulation of Electrode–Electrolyte Interactions for Improved Heat Recovery of a Thermo-Induced Electric Double-Layer Capacitor

Regulation of Electrode-Electrolyte Interactions for Improved Heat Recovery of Thermo-Induced Electric Double Layer Capacitor

Chongyan Ying [a, b], Yucheng Chen [a, b], Huachao Yang [a, b], Davide Mariotti [c], Zheng Bo [a, b, *]

[a] State Key Laboratory of Clean Energy Utilization, Institute for Thermal Power Engineering, College of Energy Engineering, Zhejiang University, 38 Zheda Road, Hangzhou, Zhejiang Province, 310027, P. R. China

[b] ZJU-Hangzhou Global Scientific and Technological Innovation Center, Hangzhou, Zhejiang Province, 311215, P. R. China

[c] Nanotechnology and Advanced Materials Research Institute, University of Ulster, Co. Antrim, BT37 0QB, UK

*Corresponding author. E-mail: bozh@zju.edu.cn

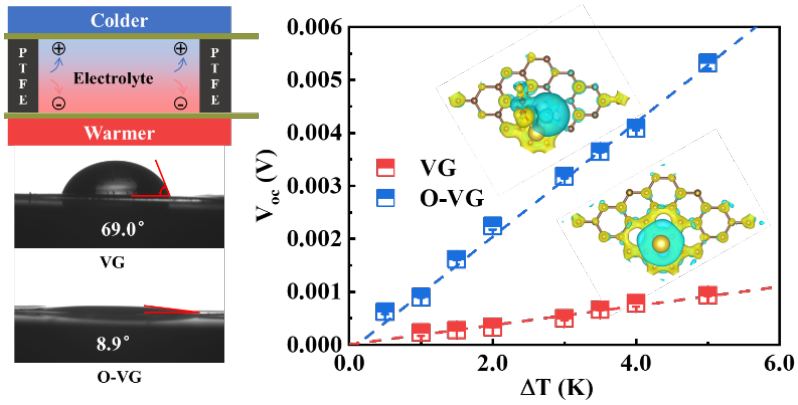

Abstract

Low-grade heat recovery through ion redistribution (i.e., Soret effect) in electric double-layer capacitors is a recent emergence for the conversion of thermal energy into electrical energy. A popular approach now in improving performance of such devices is optimizing the composition of the electrolyte. Whereas, in addition to the electrolyte ions thermodiffusion behaviors, the electrode-electrolyte interactions also play a vital role in determining the ionic Seebeck coefficient, while it has not been clearly investigated. In this work, employing vertical graphene as base material for surface modification, the crucial role of electrode-electrolyte interactions in thermoelectric conversion efficiency is demonstrated. After the surface modification via ozone treatment, oxygen-containing functional groups are enriched on graphene sheets. After improving the interfacial interactions between vertical graphene electrode and electrolyte, the ionic Seebeck coefficient is largely enhanced by 4.6 folds (up to 1 mV K^{-1}), meanwhile the capacitance is improved by 1.29 times. Density functional theory calculations reveal that such a high thermal response originates from the stronger ion-electrode interaction and the higher charge transfer efficiency via oxygen-containing functional groups. Besides, the energy stored in supercapacitors can be extracted by discharging through a resistor. The findings of this study can help for better understanding of electrode-electrolyte interactions in increasing the ionic Seebeck coefficient, providing new strategy for improved heat-to-electric conversion.

Keywords: Thermo-induced voltage; Ionic Seebeck coefficient; Electrode-electrolyte interactions; Ozone treatment; Heat recovery

1. Introduction

Electric double-layer capacitors (EDLCs) have attracted tremendous attention as energy storage devices owing to its ultra-high power density and long-term stability [1, 2]. Low-grade heat recovery by such EDLCs is also attracting attentions as a new approach to achieve waste energy harvesting. In EDLC, ion distribution in electrolytes can be influenced by the temperature gradient (i.e., Soret effect) [3, 4], which results from the inequality between ion diffusion and ion thermodiffusion contributions to the equilibrium in solution [5-7]. Onsager relations are introduced to explain such ion migration in electrolyte, which interpret the degree of ion distribution in solution is closely related to the diffusion coefficients and Eastman entropy of the ion species [5, 8]. It is worth noting that the mobility of cations and anions under the same thermal gradient is different. By using this phenomenon, a thermo-induced voltage can be generalized automatically between the negative and positive electrodes while a temperature gradient exists across the supercapacitor. According to $E = {}^{1}/_{2}\,CV^{2}$ (C is the capacitance and V is the voltage between the negative and positive electrode), it is able to improve the energy density of EDLCs via enlarged thermo-induced voltage window, therefore converting more heat energy into the electricity stored in the EDCLs [1, 7, 9, 10].

The ionic Seebeck coefficient represents the ratio of thermo-induced voltage and temperature difference. Based on the heat of ions transport in Born model [11-13], the initial contribution from one type of ions to the ionic Seebeck coefficient is relatively low, which is expected to be in the range of 0.1 mV K^{-1} [10, 11, 14]. Great efforts have been devoted to improving the performance of electrochemical thermoelectric devices from the aspect of both electrolyte and electrode [14, 15]. Optimizing the electrolyte property is a popular approach to promote the ionic Seebeck coefficient [11, 15-17]. For instance, the ratio of thermal diffusion to ion diffusion in the polyelectrolyte is proved to be much higher than that of aqueous system. This leads to a larger thermovoltage and more stable response in the polyelectrolyte [5, 11, 17, 18]. It is worth noting that the difference in the dielectric constant ($\varepsilon_{water} >> \varepsilon_{polyelectrolyte}$) cannot achieve such enhancement because heat

transfer and ion transport are both more efficient in the aqueous solution [5, 11, 18]. Besides, other methods are also applied in the electrolytes for higher and more stable energy conversion, such as importing fixed arrayed tunnels [19] and adding redox electrolytes (e.g. ferrocyanide/ferricyanide [20-22]).

On the other hand, the surface property of electrode is also critically important in determining the performance of thermoelectric supercapacitors, which are attracting more and more research interest [5, 23]. Unlike the bulk ionic thermodiffusion under a temperature gradient, ions are believed to lose part of the solvent molecular shell when contacting with the electrode surface [2, 24, 25]. The interactions at the electrode-electrolyte interface play a vital role in final thermo-induced voltage, as well as the electrosorption during this process [26, 27]. In recent reports, metals were employed as the electrode (e.g., Pt, Ni, etc.) to obtain a higher ionic Seebeck coefficient [14, 28]. It is mainly contributed by the high work function (WF) of the metal surface, which is proved to be one of the key factors for a significant thermal response [26, 28]. For example, the work function of Pt is 5.5 eV, and its ionic Seebeck coefficient can be as high as 6.5 mV K^{-1}, while the work function of In is 4.1 eV and its ionic Seebeck coefficient is only 0.5 mV K^{-1} [26]. However, the poor ion absorption capacity of pure metal is several orders of magnitude lower than those of porous active materials, which makes the pure metal uncompetitive in ionic Seebeck conversion applications.

Carbon-based materials (such as activated carbon (AC) and graphene) are emerging as the predominant alternatives of supercapacitor electrode due to the large surface area, excellent electron conductivity and chemical tunability. Energy storage capability of these materials are fundamentally based on electrosorption at electrode-electrolyte interface via an EDLC structure. Nevertheless, the ionic Seebeck coefficient is extremely low for these carbon-based materials (typically < 0.5 mV K^{-1}) [10, 14, 28]. If one can improve the ionic Seebeck coefficient of carbon materials, it can largely increase the energy density of EDLCs via recovering low-grade energy [5]. Moreover, the role and underlying mechanisms of electrolyte-electrode interactions in determining the thermo-induced voltage and heat energy conversion efficiency remain unclear [10].

In this work, the influence of electrode-electrolyte interaction on the ionic Seebeck coefficient and heat energy conversion of thermoelectric supercapacitors is comprehensively investigated. Three kinds of carbon-based materials are compared as the electrode materials to recover the heat into energy stored in EDLCs, including carbon paper, AC and vertical-oriented graphene (VG). Based on VG, the effect of surface porperty regulated by ozone treatment on the thermo-induced voltage and the heat-electricity transfer are studied. After such minor modification of oxygen-containing functional groups on graphene surface, the ionic Seebeck coefficient can be enlarged by 4.6 times to 1 mV K^{-1}, which is far beyond carbon-based materials' performance. Density functional theory (DFT) calculations are conducted to reveal the interfacial interaction between electrolyte and electrode, unveiling the underlying mechanisms of thermo-induced voltage. Furthermore, the energy stored in such EDLCs can be utilized in the discharge process through the external load.

2. Experimental and Methods

2.1. DFT calculation

The DFT calculations were implemented by VASP code with the generalized gradient approximation (GGA–PBE). The long-range interactions were described by van der Waals correction DFT-D3. A cutoff energy of 450 eV was applied in the expansion of wave functions. 9 × 9 × 1 and 25 × 25 × 1 *k*-point grids were sampled for geometry optimization and electronic property calculations. The structures of graphene models were relaxed until the convergence criteria of energy and force reach 10^{-4} eV and 10^{-3} eV $Å^{-1}$, respectively. A vacuum layer of 20 Å along the perpendicular direction was employed to minimize the image interaction. Two 2 × 2 supercells of graphene with or without carboxyl were carried out to simulate Na adsorption [29]. Based on the Bader charge analysis, the amount of charge transfer was obtained. The binding energy of Na adsorption on the graphene and modified graphene can be calculated through the following formula:

$$E_b = \left(E_{tot} - E_{graphene} - n \times E_{Na}\right)/n \quad (1)$$

where n is the number of Na atoms adsorbed on graphene, E_{tot} is the energy of graphene with adsorption, $E_{graphene}$ is the energy of graphene with or without carboxyl and E_{Na} is the energy of one sodium atom.

2.2. Device fabrication:

1 g of polyvinyl alcohol (PVA) was gradually dissolved in 10 ml of purified deionized water and the solution was stirred until the polymer was completely resolved. Then 0.2 g of NaOH pellets were gradually added and the electrolyte was then stirred at 70 ℃ until the NaOH pellets were fully dissolved. The concentrations of PVA and NaOH are 0.1 g/ml and 0.02 g/ml in electrolyte, respectively.

VG was prepared on a Ni plate (50 μm in thickness) through a plasma-enhanced chemical vapor deposition (PECVD) method. The surface wettability was regulated by ozone treatment to investigate the influence of electrode-electrolyte interactions on the thermo-induced voltage. VG was modified by functional groups under 500 ppm ozone, which was generated in a dielectric barrier discharge reactor and further humified by a water bubble column [30]. Carbon paper (HCP010N) and AC (YP-50F) are purchased from Saibo Corp.

Two VG electrodes (40 × 40 mm) were assembled with a hollow poly tetra fluoroethylene (PTFE) separation (1 mm thick, 28 × 28 mm internal size). The electrolyte was injected into this chamber and the final EDLCs device was obtained. Peltier cooler and heater were applied to produce the temperature difference across the supercapacitor. Thermocouples (TT-T-36) were fixed between the Peltier plate and electrode to measure the temperature difference across the EDLCs. Thermocouples and electrodes were separated by an insulating paper to prevent the short circuit during the test.

2.3. Thermo-induced voltage and other electrochemical measurements

The thermo-induced voltage, as well as other capacitive behaviors of supercapacitors, was recorded using an electrochemical workstation (PGSTAT302N, Metrohm Autolab B.V.). The different thermo-induced voltage tested by a two-

electrode system was derived by dividing the open-circuit voltage (V_{OC}) by the temperature difference (ΔT) across the device. The schematic illustration of the experimental setup for heat-electricity recovery is shown in Figure 1a. It is important that the ambient temperature should be maintained around 15 ℃ to avoid the disturbance caused by surrounding. During the discharge process, the temperature gradient was maintained and a 20 kΩ external resistor was loaded. The potential of the external circuit was tested by electrochemical workstation and the discharge curve of the thermo-charged capacitor was obtained.

The electrochemical characterizations, like Cyclic voltammetry (CV), Galvanostatic charge−discharge (GCD), and Electrochemical impedance spectroscopy (EIS) tests of fabricated electrodes were conducted through a two-electrodes system at room temperature. CV tests were performed in a potential window of 0-0.5 V at scan rate at 100 mV s^{-1}. GCD measurements were conducted with a potential range from 0 to 0.5 V at current densities of 0.1 mA. EIS tests were performed at the frequency range of 0.01 to 100 kHz under an amplitude of 5 mV (without any DC bias).

2.4. Materials characterizations

The morphology of the samples was conducted by scanning electron microscope (SEM, Hitachi SU-70). The contact angles of different electrodes were measured by using a DropMeter™ Professional A-200 digital goniometer in both water and electrolytes. Images of droplet impact were captured with a high-speed camera (REDLAKE MotionXtra HG-100K). X-ray photoelectron spectra (XPS) was conducted by VG ESCALAB MARK II spectrometer. Zeta potential (ζ) of electrodes was measured under 1mmol/L KCl electrolyte at pH=7 by an electrokinetic analyzer for solid surface analysis (Anton Paar SurPASS™ 3). It is worth noting that KCl solution is the standard test liquid in solid Zeta potential characterization. The work function of the VG surface was tested through Ultraviolet Photoelectron Spectrometer (UPS, Thermo ESCALAB 250XI) and analyzed by related software (Advantage 5.9). The thermal conductivity of the electrolyte was tested by a laser flash method (NETZSCH LFA467 Nanoflash) and analyzed by a fitting curve.

3. Results and discussion

3.1. Thermoelectric Performance

The schematic diagram in Figure 1a shows the experimental set-up for measuring the thermo-induced voltage. The PVA/NaOH electrolyte is filled in the cavity of the two electrodes and the temperature gradient across the supercapacitor can be mediated. The thermo-induced voltage is produced because of the ion diffusion under the temperature differences. During the diffusion process, Na^+ accumulates at the colder electrodes while the OH^- travels to the warmer electrode [11].

The heat recovery performance of three kinds of carbon materials is compared. The temperature difference ΔT across the devices is set as 1 K during the test. As shown in Figure 1b, carbon paper exhibits the highest thermo-induced voltage of 0.20 mV. The values of VG and AC are 0.19 and 0.13 mV, respectively. Notably, the duration of the three systems reaching a steady state is different from each other. VG shows the shortest time to reach the steady equilibration state (~ 23 s) in comparison with other carbon materials (~ 31 s and ~ 42 s for AC and carbon paper systems, respectively). In such electrochemical low-grade heat recovery processes, the shorter time means higher efficiency to gather heat energy. Therefore, VG is selected for the further study because of both high voltage and response speed.

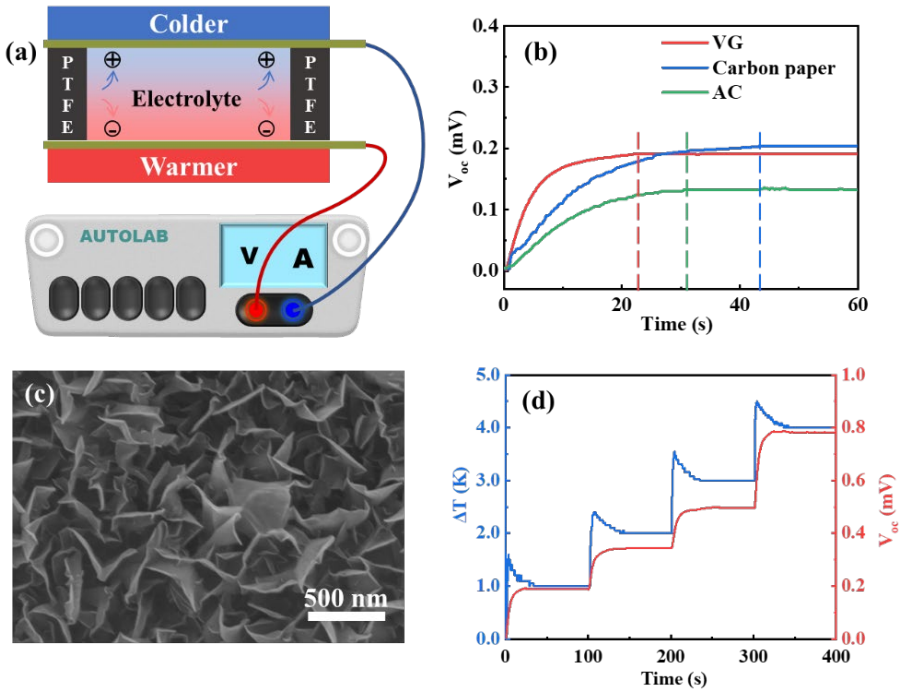

Figure 1. (a) Schematic diagram of the thermoelectric supercapacitor device and testing system. (b) Measured V_{oc} under a certain ΔT with different electrode materials. (c) Top-view SEM images of the VG electrode. (d) Measured V_{oc} and ΔT of VG sample during the heating process.

The micromorphology of VG is characterized by SEM. As displayed in Figure 1c, VG is composed of dense graphene petals with exposed edges. The nanoscale 3D porous structure provides open channels and abundant surface for fast ion diffusion and adsorption. At any given ΔT applied by Peltier plate, the corresponding thermo-induced voltage can be tested. As shown in Figure 1d, when the ΔT is set as 1 K, the V_{oc} of VG-based supercapacitor rapidly increases to 0.19 mV. The steady state can be held with controlling temperature difference. With the ΔT gradually increasing to 4 K, the thermo-induced voltage can be prominently enlarged to 0.78 mV. Based on the V_{oc} change, the ionic thermoelectric coefficient of linear fitted $V_{oc}/\Delta T$ can be calculated (0.18 mV K^{-1}).

3.2. Regulation of surface properties

The surface wettability of VG is modified by ozone treatment. As shown in Figure 2a, the O peak at around 531 eV and 739 eV can be observed on VG sample (O-VG) in XPS spectra after ozone treatment. The XPS result suggests that oxygen-containing functional groups are enriched on the VG surface. Then, water contact angles are

measured to characterize the surface wettability. The optical microscope images are recorded at 40 s after the deionized water droplet is contacted with the VG and O-VG samples. As shown in Figure 2b, the equilibrium apparent contact angle of the pure VG is measured to be 106.2°, indicating the hydrophobic nature. After the ozone treatment, the contact angle is reduced to 33.5° for the O-VG, which suggests the hydrophilic property. Subsequently, the surface wettability for PVA electrolyte is also detected. As shown in Figure 2c, the contact angles of VG and O-VG are measured to be 69.0° and 8.9°, respectively. Importantly, the reduced contact angle after the ozone treatment demonstrates that the wetting performance can be improved through the ozone treatment. Therefore, the electrolyte can spread swiftly on the O-VG surface. Besides, the contact angle of PVA electrolyte is smaller than that of deionized water, which is due to the lower polarity of PVA. Compared with aqueous liquid, improved surface wettability yields stronger electrode-electrolyte interactions, thereby also contributing to higher thermal response voltage.

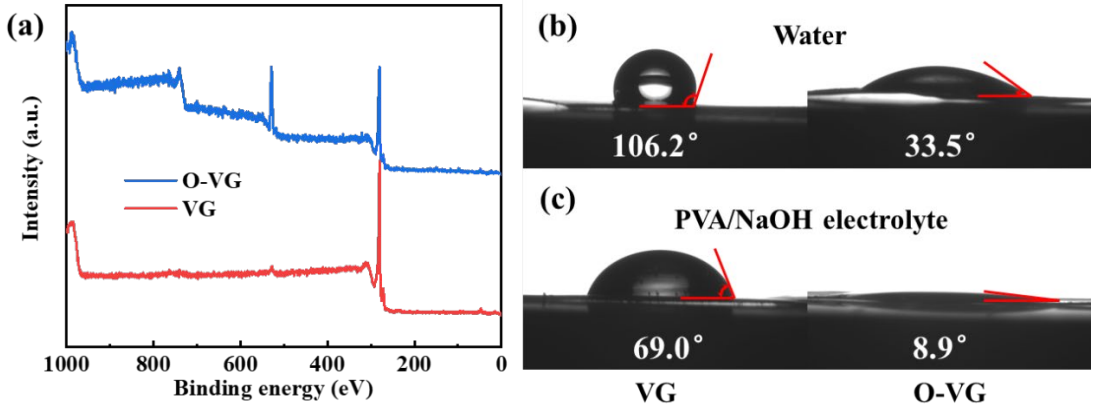

Figure 2. (a) XPS spectra of VG before and after surface ozone treatment. The apparent contact angle of VG and O-VG with (b) water and (c) PVA electrolyte.

Depending on the surface chemistry and polarity, the surface charges on the graphene affect the graphene-ion interactions in the electrolyte. To experimentally confirm the enhancement of surface charges of graphene after ozone treatment, the zeta potentials of two electrodes are measured and compared. As shown in Figure 3, the zeta potential of O-VG (-61.4 mV) is much larger than that of original VG electrode (-42.1

mV), suggesting the improved negative charges on the O-VG surface. A more negative value of the electric potential is beneficial for ion absorption at the O-VG surface.

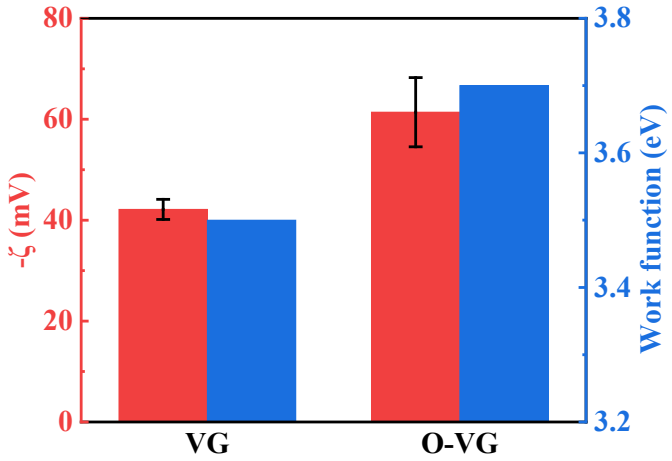

Figure 3. Zeta potential and WF value of VG and O-VG.

To further investigate the surface properties of VG and O-VG, work functions (WF) of the samples are detected (see the blue bars in Figure 3). According to the UPS test, the WF values of VG and O-VG are measured to be 3.5 and 3.7 eV, respectively. The WF values of graphene electrodes are closely related to the ionization energy and surface charges [26]. Such results are accordant with the Zeta potential of two electrodes that O-VG with a more negative charge has a higher WF value. Also, the WF value and corresponding ionic Seebeck coefficient of VG electrode are lower than those of pure metals (e.g., Pt), suggesting that WF is correlated to the thermal response of thermo-induced EDLCs.

3.3. Electrochemical performance

The super-hydrophilic property of the O-VG surface makes a great contribution to electrochemical performance. Figure 4a shows the CV curves of VG and O-VG electrodes at a scan rate of 100 mV s^{-1}. Two CV curves present a similar rectangular shape, indicating the ideal EDLC behavior. Based on the CV curves, the specific capacitance of fabricated supercapacitor was calculated by:

$$C_{cv} = \int IdV/(v \times \Delta V), \quad (2)$$

where I is the response current (A), v and ΔV are the potential scan rate (100 mV s^{-1}) and the potential window (V), respectively. Notably, the CV integration area of O-VG, corresponding to a capacitance of 2.31 mF at 100 mV s^{-1}, is greater than that of VG (1.79 mF). Such a significant improvement can be attributed to the improved wettability which renders electrolytes readily penetrate the spaces between the adjacent graphene petals for higher capacitance.

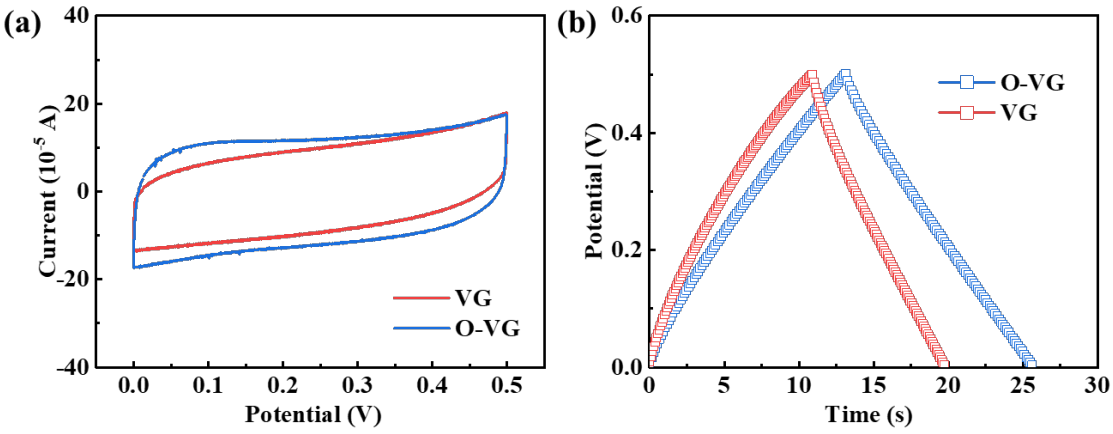

Figure 4. (a) CV curves at 100 mV s^{-1} for VG and O-VG. (b) GCD plots for two electrodes under 0.1 mA.

Similar results can be found in the GCD tests in Figure 4b. According to the GCD electrochemical test, C_{GCD} derived from GCD tests can be calculated by:

$$C_{GCD} = {It}/{U}, \tag{3}$$

where I is the applied current (A), t is the discharging time (s), and U is the potential window excluding IR drop in the discharge process (V). The capacitances based on the GCD tests are measured to be 1.81 and 2.53 mF for the VG and O-VG electrodes, respectively. Apparently, the capacitance is enhanced after the ozone treatment, which is consistent with the results of CV tests.

The electrolyte transport properties are characterized by electrochemical impedance spectroscopy (EIS). As shown in Figure 5a, the impedance of VG and O-VG electrodes consists of two parts, including a distorted quasi-semicircle in the high-frequency region (inset of Figure 5a) and a quasilinear part in the low-frequency region. The intercept on X-axis indicates the equivalent series resistance (ESR), which

corresponds to the electrode ionic resistance. The ESR value decreases from 23.1 to 17.5 Ω with the functional groups modified on the graphene surface. At the low-frequency region of Nyquist spectra, the circuit can be regarded as an RC circuit. The resistance originates from the ion diffusion in the electrolyte and interfacial impedance at the electrode surface [31]. At the low-frequency region, the slope of O-VG is slightly larger than that of VG, representing a lower equivalent resistance. Considering the same electrolyte environment in the test system, such difference is primarily attributed to the interfacial impedance, indicating that the oxygen-containing functional groups on graphene significantly reduce the interfacial resistance of ion adsorption and desorption.

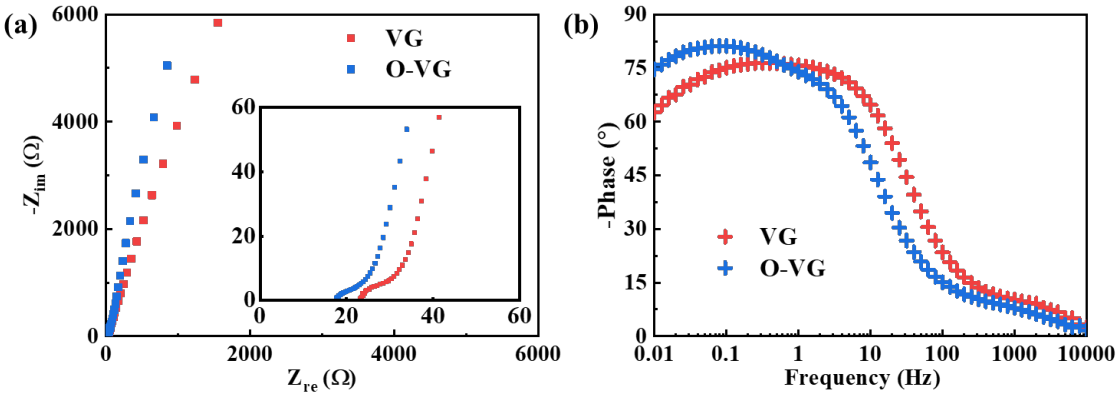

Figure 5. (a) Nyquist plots of VG and O-VG electrodes; the inset denotes the magnification of the high-frequency region. (b) Bode plots of two electrodes.

Figure 5b illustrates the phase angle versus frequency. In general, a higher phase angle is indicative of better ion adsorption/desorption behavior at the interface. The maximum phase angle in the Bode plots for the O-VG electrode is 81.2°, which is higher than that of VG electrode (76.5°). Such an increase in maximum phase angle after ozone treatment indicates an improved energy storage performance. Moreover, the phase angle at the low-frequency region of O-VG (74.6° at 0.01 Hz) is slightly larger than that of VG (62.6° at 0.01 Hz), which signifies a better capacitance performance in that region.

3.4. Thermo-induced voltage

The ionic thermoelectric coefficient is also prominently improved after the ozone treatment, suggesting that strong electrode-electrolyte interactions benefits high thermo-induced voltage. A comparison of two electrodes in the ionic thermoelectric phenomenon is carried out. As is shown in Figure 6a, a 4 K temperature gradient is applied across the supercapacitors. The O-VG supercapacitor is thermo-charged to 4.1 mV while that of VG-based supercapacitor is only 0.8 mV.

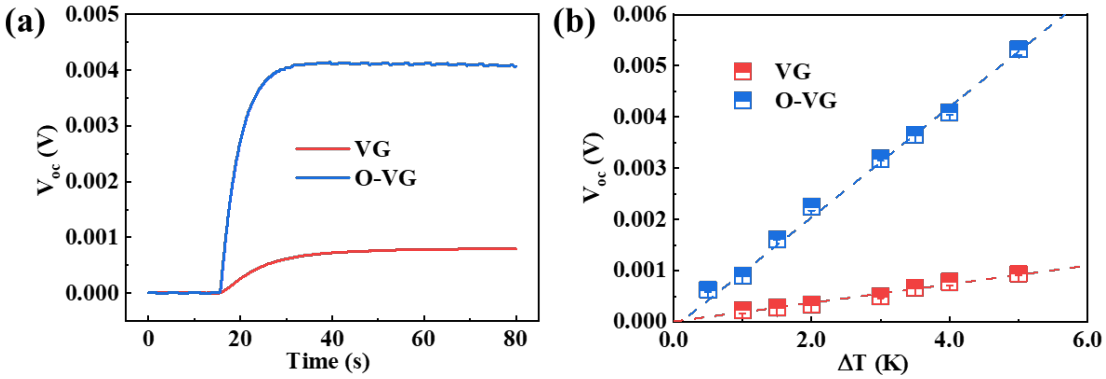

Figure 6. (a) The measured V_{oc} during the heating process. (b) V_{oc} at different ΔT values and the linear fitting curves of VG and O-VG electrodes.

The experimental V_{oc} value of two electrodes under different temperature gradients is plotted in Figure 6b. According to the slope of the linear fit, the ionic Seebeck coefficient of VG is 0.18 mV K^{-1}. As for the O-VG electrode, a significant improvement of thermoelectric coefficient can be obtained (1 mV K^{-1}), which is 5.6 folds higher than that of VG counterpart. Combined with the zeta potential and work function results, oxygen-containing functional groups greatly promote the interfacial interaction between electrolyte and electrode, demonstrating that surface properties play a vital role in determining the heat-electricity recovery.

To further reveal the underlying mechanisms, the binding energy of Na and two kinds of electrodes are carried out by DFT simulations. With the absorption of Na, the binding energy E_b of Na is shown in Figure 7a. The E_b between Na and VG is calculated to be -0.15 eV, which is much lower than that of O-VG (-1.51 eV). Such an obvious difference explains the stronger interaction between functionalized graphene and Na, which further contribute to a higher response voltage in thermo-induced EDLC. With

the further increase in the Na absorption, E_b between Na and graphene (VG) slightly increases to -0.6 eV while E_b of O-VG gradually reduces to -0.74 eV. This is because the interaction among Na plays a dominant role with adding more atoms, meanwhile the binding energy E_b between Na and graphene is no longer predominantly dominant in the system. The divergence of E_b between VG and O-VG demonstrates that the interaction between electrolyte ions and functionalized graphene is stronger than that of pristine graphene.

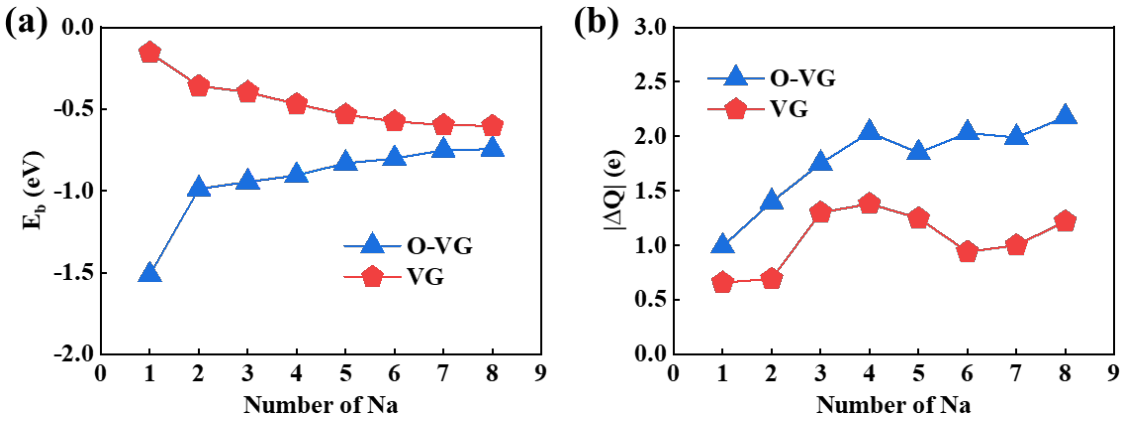

Figure 7. (a) The binding energy E_b with the increasing number of Na absorption. (b) The amount of charge transfer with the increasing number of Na absorption.

The amount of surface charge transfer of two electrodes during the absorption is compared in Figure 7b. It can be seen that the amount of charge transfer of O-VG is significantly larger than that of VG. The charge transfer number of the first Na absorbed on O-VG is about 1.0 *e*, indicating that it is almost entirely oxidized. As for VG, the amount of charge transfer is approximately 0.6 *e*. With an increasing number of absorbed Na, the charge transfer number rises from 1.0 to approximately 2.0 *e* on O-VG, while it fluctuates around 1.0 *e* on VG. It is worth noting that there is no more significant improvement of charge transfer on O-VG because of the restriction carboxyl number in the model. According to the DFT calculations, the charge transfer number of O-VG is almost two times that of VG, which can be attributed to the oxygen-containing functional groups on VG that can provide more active electron acceptors. Based on these results, more charges can be transferred on O-VG when adsorbing the same

number of ions, which means the efficiency of charge transfer on the O-VG surface is much higher than that of VG counterpart.

During the process of Na absorption, the difference of the density of states are shown in Figure 8. The Fermi level (E_f) of VG and O-VG are calculated to be -2.86 and -2.9 eV, respectively. The E_f of O-VG is slightly larger than that of VG, which is accordance to the WF test. Compared with pure VG, the functional group modification induces a higher density of states around the Fermi level ($E- E_f=0$ eV), which indicates that O-VG has higher reactivity and conductivity. With the absorption of Na on the graphene surface, the Fermi level of two systems both have an upward trend, and the curves show a shift to left. In regard to VG, the absorbed Na of O-VG system introduces more orbitals at higher energy levels and more distortions of band structures, which is contributed to stronger bonding between O-VG and Na.

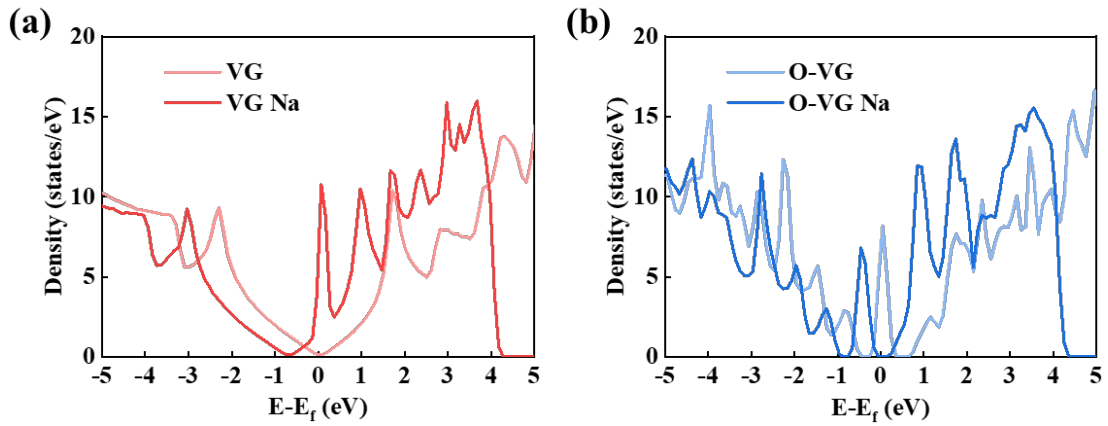

Figure 8. The density of states of VG (a) and O-VG (b) in the process of Na absorption.

Figure 9 exhibits the deformation charge density of two systems. The yellow and blue areas represent charge accumulation and depletion, respectively. Figure 9a and c (VG system) show that the charges are localized evenly at carbon atom on the graphene surface and enriched around carbon atoms near Na atom. And the Na atom and the graphene are separated by an electron-deficient region. Such results indicate that the ionized Na atom are combined with graphene in the form of electrostatic adsorption. In Figure 9b and d (O-VG system), the charge is mainly accumulated between Na and the oxygen-containing functional group and charge depletion can be seen around Na atom,

which means that the ionized Na atom is adsorbed on the surface of O-VG through chemical bonds.

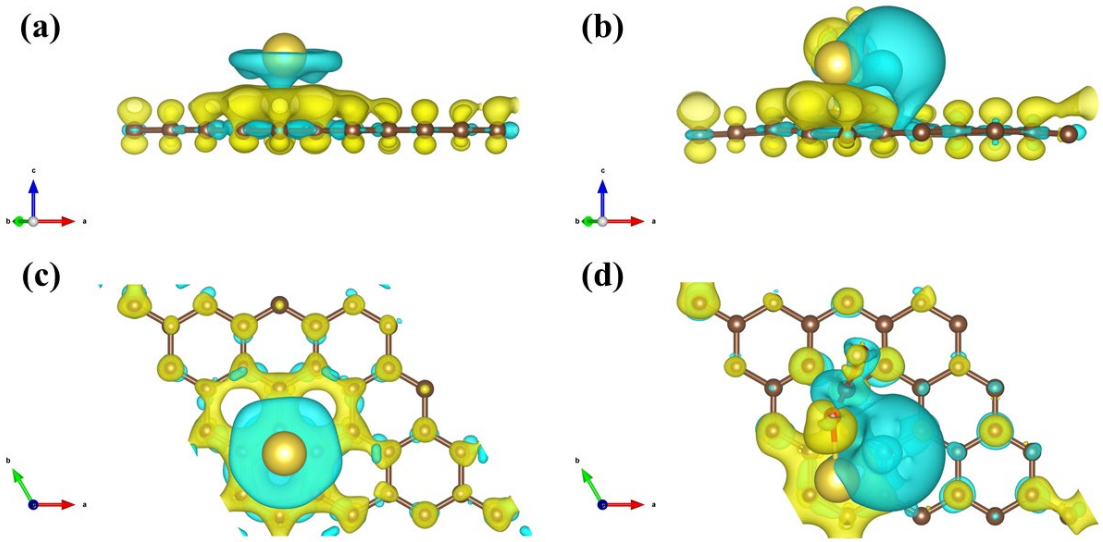

Figure 9. The deformation charge density of Na absorbed on VG (a, c) and O-VG (b, d).

By connecting an external load resistor (20 kΩ in current experiment), the thermo-induced voltage can be discharged, which can simulate the practical application of the stored energy. Discharged curves of VG and O-VG EDLCs are exhibited in Figure 10. According to the resistor-capacitor (RC) circuit theory, the instant potential change of the resistor can be fitted by:

$$V_t = V_0 \cdot exp(-t/RC) \quad (4)$$

where V_t is the voltage across the capacitor at elapsed time t during discharging, V_0 is the initial voltage of the capacitor, R is the external resistor (20 kΩ), C is the capacitance of the capacitor. Based on the RC discharging circuit (Eq. 4), the capacitance of VG-based supercapacitor is 1.86 mF while the capacitance of O-VG is 2.32 mF, which is also consistent with the experimental results by CV and GCD. It is also worth noting that this capacitance is orders of magnitude larger than that of normal metal electrodes [5, 10, 11, 28].

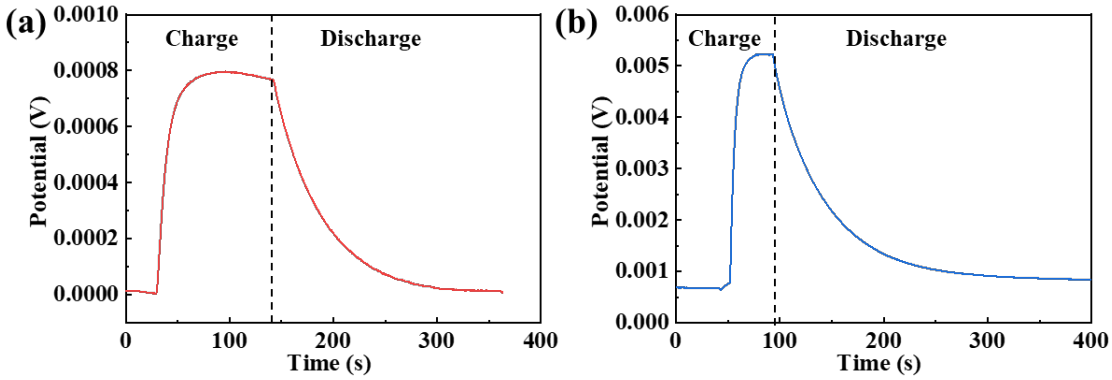

Figure 10. The thermo-charging and discharging curves of VG (a) and O-VG (b) supercapacitors.

Importantly, ~4.6-fold increase in the ionic Seebeck coefficient is achieved after regulating the electrode-electrolyte interactions via the surface functional groups, which greatly improves the thermoelectric efficiency. The efficiency (η) of thermo-induced EDLC is calculated through the fitting curve to further evaluate the performance of thermo-induced EDLCs. The energy conversion efficiency is defined as

$$\eta = {}^{E_C}/_{Q_{in}} \tag{5}$$

where E_c and Q_{in} are energy stored in EDLC and the thermal energy conducted through the device, respectively. In Eq. 5,

$$E_C = {}^1/_2\, CV^2 = {}^1/_2\, C\alpha^2\Delta T^2 \tag{6}$$

$$Q_{in} = kA\Delta t\Delta T/l \tag{7}$$

where α represents the ionic Seebeck coefficient (mV K^{-1} or V K^{-1}), k is the thermal conductivity of electrolyte between two electrodes (W m^{-1} K^{-1}), Δt is the charging time from 0 to a steady state (s), A and l are the effective area (m^2) of the electrode and the thickness (m) of the central block (PTFE separation), respectively.

PVA/NaOH electrolyte exhibits a low thermal conductivity of 0.47 W m^{-1} K^{-1}, corresponding to the electrical energy of 6.0×10^{-10} J after a single thermal charge. The η of VG electrode is calculated to be 2.0×10^{-9} under the circumstance of ΔT = 4 K, while the efficiency of O-VG is as high as 6.7×10^{-8}. Such great improvement (~34 times) is primarily attributed to the increased capacitance and ionic Seebeck coefficient.

4. Conclusion

In conclusion, using interface control strategy to modify the graphene surface provides a promising solution for increasing the thermo-induced voltage of graphene electrodes in low-grade heat recovery by EDLC. After ozone treatments, the intrinsically hydrophobic graphene surface changes to hydrophilic and the surface properties of zeta potential, and the work function is improved. Benefiting from such increased binding energy and larger active surface area, the capacitance of EDLC is slightly expanded (1.29 folds). In terms of the thermal-induced voltage response, the ionic Seebeck coefficient of graphene electrode after surface modification can achieve 1 mV K^{-1} (~4.6 times larger than before). DFT simulation results illustrate that such remarkable enhancement is attributed to enhanced interfacial interaction with ion absorption and higher charge transfer efficiency, which promotes the response voltage and energy storage in the heat-electricity process. This work demonstrates the importance of interfacial interaction and electrode properties in electrochemical low-grade heat recovery and proposes an approach to improve the practical performance of thermal-induced electric double-layer capacitors.

Corresponding Author

Zheng Bo [a, b, *]

[a] State Key Laboratory of Clean Energy Utilization, Institute for Thermal Power Engineering, College of Energy Engineering, Zhejiang University, 38 Zheda Road, Hangzhou, Zhejiang Province, 310027, P. R. China

[b] ZJU-Hangzhou Global Scientific and Technological Innovation Center, Hangzhou, Zhejiang Province, 311215, P. R. China

E-mail：bozh@zju.edu.cn

Notes

The authors declare that there is no conflict of interests.

Acknowledgment

The authors would like to thank the financial support from the National Natural Science Foundation of China (No. 51906211), the Royal Society Newton Advanced Fellowship (No. 52061130218), the Key R&D Program of Zhejiang Province (No. 2019C01044), and the Zhejiang Provincial Natural Science Foundation of China (No. LR17E060002).

References

(1) Härtel, A.; Janssen, M.; Weingarth, D.; Presser, V.; van Roij, R. Heat-to-current conversion of low-grade heat from a thermocapacitive cycle by supercapacitors. *Energy Environ. Sci.* **2015**, *8* (8), 2396-2401. DOI: 10.1039/C5EE01192B.

(2) Simon, P.; Gogotsi, Y. Perspectives for electrochemical capacitors and related devices. *Nat. Mater.* **2020**, *19* (11), 1151-1163. DOI: 10.1038/s41563-020-0747-z.

(3) Rahman, M. A.; Saghir, M. Z. Thermodiffusion or Soret effect: Historical review. *Int. J. Heat Mass Transf.* **2014**, *73*, 693-705. DOI: 10.1016/j.ijheatmasstransfer.2014.02.057.

(4) Tyrrell, H. J. V.; Taylor, D. A.; Williams, C. M. The 'Seebeck Effect' in a Purely Ionic System. *Nature* **1956**, *177* (4510), 668-669. DOI: 10.1038/177668b0.

(5) Han, C.-G.; Qian, X.; Li, Q.; Deng, B.; Zhu, Y.; Han, Z.; Zhang, W.; Wang, W.; Feng, S.-P.; Chen, G.; Liu, W. Giant thermopower of ionic gelatin near room temperature. *Science* **2020**, *368* (6495), 1091. DOI: 10.1126/science.aaz5045.

(6) Gao, C.; Lee, S. W.; Yang, Y. Thermally Regenerative Electrochemical Cycle for Low-Grade Heat Harvesting. *ACS Energy Lett.* **2017**, *2* (10), 2326-2334. DOI: 10.1021/acsenergylett.7b00568.

(7) Kim, S. L.; Lin, H. T.; Yu, C. Thermally Chargeable Solid-State Supercapacitor. *Adv. Energy Mater.* **2016**, *6* (18), 1600546. DOI: 10.1002/aenm.201600546.

(8) Eastman, E. D. THEORY OF THE SORET EFFECT. *J. Am. Chem. Soc.* **1928**, *50* (2), 283-291. DOI: 10.1021/ja01389a007.

(9) Rahimi, M.; Straub, A. P.; Zhang, F.; Zhu, X.; Elimelech, M.; Gorski, C. A.; Logan, B. E. Emerging electrochemical and membrane-based systems to convert low-grade heat to electricity. *Energy Environ. Sci.* **2018**, *11* (2), 276-285. DOI: 10.1039/C7EE03026F.

(10) Al-zubaidi, A.; Ji, X.; Yu, J. Thermal charging of supercapacitors: a perspective. *Sustain. Energ. Fuels* **2017**, *1* (7), 1457-1474. DOI: 10.1039/c7se00239d.

(11) Zhao, D.; Wang, H.; Khan, Z. U.; Chen, J. C.; Gabrielsson, R.; Jonsson, M. P.; Berggren, M.; Crispin, X. Ionic thermoelectric supercapacitors. *Energy Environ. Sci.* **2016**, *9* (4), 1450-1457, 10.1039/C6EE00121A. DOI: 10.1039/C6EE00121A.

(12) Petit, C. J.; Renner, K. E.; Lin, J. L. The entropy of transport of sodium chloride and potassium chloride at 30.degree.C. *J. Phys. Chem.* **1984**, *88* (12), 2435-2436. DOI: 10.1021/j150656a004.

(13) Agar, J. N.; Mou, C. Y.; Lin, J. L. Single-ion heat of transport in electrolyte solutions: a hydrodynamic theory. *J. Phys. Chem.* **1989**, *93* (5), 2079-2082. DOI: 10.1021/j100342a073.

(14) Lim, H.; Lu, W.; Chen, X.; Qiao, Y. Effects of ion concentration on thermally-chargeable double-layer supercapacitors. *Nanotechnology* **2013**, *24* (46), 465401. DOI: 10.1088/0957-4484/24/46/465401.

(15) Yu, B.; Duan, J.; Cong, H.; Xie, W.; Liu, R.; Zhuang, X.; Wang, H.; Qi, B.; Xu, M.; Wang, Z. L.; Zhou, J. Thermosensitive crystallization–boosted liquid thermocells for low-grade heat harvesting. *Science* **2020**, *370* (6514), 342. DOI: 10.1126/science.abd6749.

(16) Cheng, H.; He, X.; Fan, Z.; Ouyang, J. Flexible Quasi-Solid State Ionogels with Remarkable Seebeck Coefficient and High Thermoelectric Properties. *Adv. Energy Mater.* **2019**, *9*, 1901085. DOI: 10.1002/aenm.201901085.

(17) Brogioli, D.; La mantia, F. Heat recovery in energy production from low temperature heat sources. *AICHE J.* **2019**, *65* (3), 980-991. DOI: 10.1002/aic.16496.

(18) Bonetti, M.; Nakamae, S.; Roger, M.; Guenoun, P. Huge Seebeck coefficients in nonaqueous electrolytes. *J. Chem. Phys.* **2011**, *134* (11), 114513. DOI: 10.1063/1.3561735.

(19) Li, T.; Zhang, X.; Lacey, S. D.; Mi, R.; Zhao, X.; Jiang, F.; Song, J.; Liu, Z.; Chen, G.; Dai, J.; Yao, Y.; Das, S.; Yang, R.; Briber, R. M.; Hu, L. Cellulose ionic conductors with high differential thermal voltage for low-grade heat harvesting. *Nat. Mater.* **2019**, *18* (6), 608-613. DOI: 10.1038/s41563-019-0315-6.

(20) Qian, G.; Yu, X.; Li, Z.; Wu, J.; Huang, R.; Lu, Y. Experimental investigation of a U-tube thermocell under various Fe(CN)63−/4− concentration. *Energy Conv. Manag.* **2020**, *217*, 113005. DOI: 10.1016/j.enconman.2020.113005.

(21) Kundu, A.; Fisher, T. S. Harnessing the thermogalvanic effect of the ferro/ferricyanide redox couple in a thermally chargeable supercapacitor. *Electrochim. Acta* **2018**, *281*, 357-369. DOI: 10.1016/j.electacta.2018.05.164.

(22) Dupont, M. F.; MacFarlane, D. R.; Pringle, J. M. Thermo-electrochemical cells for waste heat harvesting – progress and perspectives. *Chem. Commun.* **2017**, *53* (47), 6288-6302. DOI: 10.1039/C7CC02160G.

(23) Im, H.; Kim, T.; Song, H.; Choi, J.; Park, J. S.; Ovalle-Robles, R.; Yang, H. D.; Kihm, K. D.; Baughman, R. H.; Lee, H. H.; Kang, T. J.; Kim, Y. H. High-efficiency electrochemical thermal energy harvester using carbon nanotube aerogel sheet electrodes. *Nat. Commun.* **2016**, *7*, 10600. DOI: 10.1038/ncomms10600.

(24) Chmiola, J.; Yushin, G.; Gogotsi, Y.; Portet, C.; Simon, P.; Taberna, P. L. Anomalous Increase in Carbon Capacitance at Pore Sizes Less Than 1 Nanometer. *Science* **2006**, *313* (5794), 1760. DOI: 10.1126/science.1132195.

(25) Kong, J.; Yang, H.; Guo, X.; Yang, S.; Huang, Z.; Lu, X.; Bo, Z.; Yan, J.; Cen, K.; Ostrikov, K. K. High-Mass-Loading Porous Ti3C2Tx Films for Ultrahigh-Rate Pseudocapacitors. *ACS Energy Lett.* **2020**, *5* (7), 2266-2274. DOI: 10.1021/acsenergylett.0c00704.

(26) Lim, H.; Shi, Y.; Wang, M.; Qiao, Y. Effects of work function on thermal sensitivity of electrode potential. *Appl. Phys. Lett.* **2015**, *106* (22), 223901. DOI: 10.1063/1.4921769.

(27) Liu, A. T.; Zhang, G.; Cottrill, A. L.; Kunai, Y.; Kaplan, A.; Liu, P.; Koman, V. B.; Strano, M. S. Direct Electricity Generation Mediated by Molecular Interactions with Low Dimensional Carbon Materials-A Mechanistic Perspective. *Adv. Energy Mater.* **2018**, *8* (35), 1802212. DOI: 10.1002/aenm.201802212.

(28) Bonetti, M.; Nakamae, S.; Huang, B. T.; Salez, T. J.; Wiertel-Gasquet, C.; Roger, M. Thermoelectric energy recovery at ionic-liquid/electrode interface. *J. Chem. Phys.* **2015**, *142* (24), 244708. DOI: 10.1063/1.4923199.

(29) Xu, Z.; Yue, M.; Chen, L.; Zhou, B.; Shan, M.; Niu, J.; Li, B.; Qian, X. A facile preparation of edge etching, porous and highly reactive graphene nanosheets via ozone treatment at a moderate temperature. *Chem. Eng. J.* **2014**, *240*, 187-194. DOI: 10.1016/j.cej.2013.11.045.

(30) Yang, S.; Bo, Z.; Yang, H.; Shuai, X.; Qi, H.; Li, X.; Yan, J.; Cen, K. Hierarchical Petal-on-Petal MnO2/Vertical Graphene Foam for Postplasma Catalytic Decomposition of Toluene with High Efficiency and Ultralow Pressure Drop. *Ind. Eng. Chem. Res.* **2018**, *57* (45), 15291-15300. DOI: 10.1021/acs.iecr.8b03387.

(31) Mathis, T. S.; Kurra, N.; Wang, X.; Pinto, D.; Simon, P.; Gogotsi, Y. Energy Storage Data Reporting in Perspective—Guidelines for Interpreting the Performance of Electrochemical Energy Storage Systems. *Adv. Energy Mater.* **2019**, *9* (39), 1902007. DOI: 10.1002/aenm.201902007.